

Altermagnetic phases and phase transitions in Lieb-5 Hubbard model

Sougata Biswas , ^{1,*} Achintyaa , ^{1,2,†} and Paramita Dutta , ^{1,‡}

¹ Theoretical Physics Division, Physical Research Laboratory,
Navrangpura, Ahmedabad, Gujarat-380009, India

² Indian Institute of Technology Gandhinagar, Palaj, Gujarat-382055, India

The emergence of altermagnetism, the collinear magnetic phase characterized by momentum-dependent spin-split bands but zero net magnetization, has fundamentally reshaped the classification of magnetic order. We propose an altermagnetic (AM) order in a repulsive Hubbard model on the Lieb-5 lattice. Considering only nearest-neighbor hoppings within the lattice, we show a phase transition from the nonmagnetic to a unique AM isolated band metal phase (AMIM), allowing clear identification of spin-split states. Additionally, the AM metallic phase (AMM) is also shown to appear as an intermediate phase during the transition from the normal metal to the AMIM in the presence of the diagonal hopping within each unit cell of the Lieb-5 lattice. The manifestation of distinct AM phases and the phase transitions, driven by Hubbard interaction and hopping integrals, have been explored in terms of spin-resolved band structure, spectral function, and the behavior of the AM order parameter. The stability of these AM phases against the spin-orbit coupling and temperature is also established.

INTRODUCTION

Magnetic materials are traditionally classified into two primary types based on the spin ordering. Ferromagnets (FM) host spin-split energy bands with a finite magnetic moment originating from the parallel alignment of spins. Antiferromagnets (AFM) in which neighboring spins align antiparallel, possess zero net magnetization, and exhibit spin-degenerate energy bands. Beyond this traditional classification of magnetism, a new class of two-dimensional (2D) magnetic order, termed as ‘altermagnetism’, has been recently identified [1–18]. The momentum-dependent spin-splitting of the energy bands together with the zero net magnetization property makes the altermagnet (AM) to partially share characteristics of both FM and AFM, yet remain fundamentally distinct from either [9–11, 17, 18]. The cancellation of the net magnetization in AMs arises from the alternating spin orientation on neighboring two sublattices with broken Kramer’s spin-degeneracy [15, 19]. However, unlike in conventional AFM, these opposite spin sublattices follow a specific crystal rotation that is inherent to the lattice symmetry [20, 21].

Owing to the unique combination of FM-like spin splitting and AFM-like zero net magnetization, AMs support strong spin currents, high-frequency dynamics with minimum stray field [22, 23]. AM phases have been realized experimentally in a wide range of materials starting from RuO₂ [24–28], and extended to CrSb [29–32], K-Cl [33, 34], MnTe [15, 19, 35, 36], MnF₂ [3, 37], FeSb₂ [7], GdAlSi [38], KV₂Se₂O [39], and others [40, 41]. They have emerged as promising materials, exhibiting a wide range of intriguing physical properties including superconductivity [42–61], magnetoresistance [12, 14, 62, 63], topological phases [53, 64, 65] with potential of applications in spintronics [66–71] and other fields [13, 18, 27, 72–77].

Altermagnetic phases have been investigated across a variety of lattice models: square lattice [20, 21, 78–

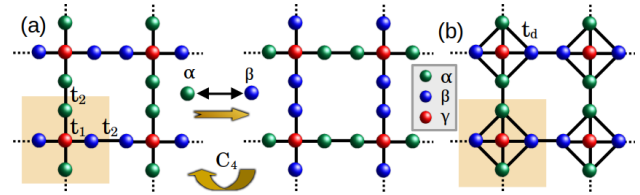


FIG. 1: (a) Lieb-5 lattice containing three sub-lattices invariant under a spin flip followed by a C_4 rotation around the center. (b) Its variant with diagonal hopping.

80], Shastry-Sutherland lattice [81], square-octagon lattice [21, 59, 82, 83], hexa-triangular lattice [79], honeycomb lattice [82, 84], Kondo lattice [43], and others [21, 82, 85], demonstrating how crystal symmetries combined with appropriate spin distribution can give rise to alternating spin polarization and spin-split band structures without net magnetization in various ways. Depending on the local environment and the strength of the interaction, these lattices have been found to exhibit altermagnetic-metallic (AMM) or an altermagnetic-insulating (AMI) phase [20, 78]. Among various lattices, the traditional Lieb lattice, often regarded as a prototype for oxychalcogenides or anti-CuO₂ materials [86, 87], has drawn attention because of the simplicity of the lattice being very close to the square lattice model. The Lieb lattice, characterized by various electronic and topological features arising from its extended structural connectivity, has served as an important model for exploring various physical phenomena. These include localization-delocalization properties [88–92], topological phases and edge states [93–99], magnetic phases [100–104], and superconducting phases [105–107]. Lieb lattices have been realized experimentally [21, 108–115] showcasing the potential of application across various fields [108, 109, 116–121]. The AM phase in this lattice has been shown to arise from the coexistence of magnetic and non-magnetic

sites at specific Wyckoff positions [86, 87].

In this article, we demonstrate a new type of AM phase, *altermagnetic isolated band metal (AMIM) phase and also AMM phase, and their transitions in Lieb-5 lattice* based on a repulsive Hubbard model. In contrast to the AMM phase found in the traditional Lieb (also known as Lieb-3) metal [21, 86, 87], we show a unique AM phase in the Lieb-5 Hubbard model within a minimum local atmosphere (without any diagonal hopping). We establish the AM phase in our model by investigating the behavior of the spin-resolved band structure and spectral density function. Inclusion of the next-nearest neighbor hopping integral allows us to further control the phase diagram. The effect of the intrinsic spin-orbit coupling has also been studied to explore the stability of the AM phases in the present lattice. The simplicity of our lattice model showing multiple AM phases, including the unique AMIM phase, even without any second-neighbor interaction term, enhances the importance of the present work.

MODEL AND METHOD

We consider a repulsive Hubbard model in a 2D Lieb-5 lattice consisting of three sublattices, α , β , and γ , within a unit cell as shown in Fig. 1 (yellow-shaded area). The Hamiltonian reads,

$$\mathcal{H} = - \sum_{i,j,\sigma} t_{ij} (c_{i\sigma}^\dagger c_{j\sigma} + h.c.) + U \sum_{i \in \alpha, \beta} n_{i\uparrow} n_{i\downarrow} + \varepsilon \sum_{i,\sigma} n_{i\sigma}, \quad (1)$$

where $c_{i,\sigma}^\dagger$ ($c_{i,\sigma}$) operator creates (annihilates) an electron of spin σ ($=\uparrow, \downarrow$) at i -th site. The hopping integral t_{ij} can take values t_1 and t_2 for the intracell and intercell hopping, respectively, whereas, the diagonal hopping is denoted by t_d . The term ε is the onsite potential fixed to zero for all sublattices throughout our calculations. The repulsive Hubbard interaction is introduced through the second term of Eq. 1 with U as the on-site interaction strength, but only at α and β sublattices; the sublattice γ being free from the interaction. The system can return to its original configuration when two consecutive transformations (*i*) spin flip between α and β sublattices (exchanging green and blue sites) and (*ii*) $[C_4]$ rotation about the γ site are applied.

In order to investigate the magnetic order, we carry out a self-consistent Hartree–Fock (HF) analysis which captures the onset of magnetic phases decided by the underlying lattice geometry and interaction strength. The AM order parameter (δm) proportional to the staggered magnetization can be defined as [20]

$$\delta m = \frac{1}{8N} \left\langle \sum_{i \in \alpha} (n_{i\uparrow} - n_{i\downarrow}) - \sum_{i \in \beta} (n_{i\uparrow} - n_{i\downarrow}) \right\rangle_{HF} \quad (2)$$

ensuring the finite contribution from the α and β sublattices and no role of γ sublattice; N being the total

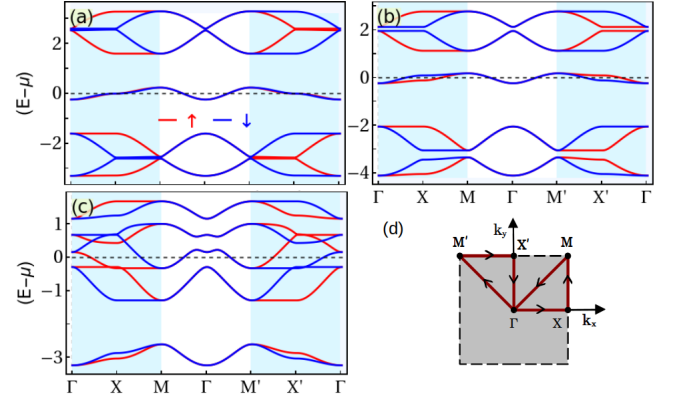


FIG. 2: Spin-resolved band structure of Lieb-5 lattice in the AM phase (a) without ($t_d = 0$) and (b,c) with diagonal hopping ($t_d = 0.5$). The Hubbard interaction term is considered as (a,b) $U = 5$ and (c) $U = 3$. The other parameters are: $t_1 = 1$, $t_2 = 0.5$, $T = 0$. (d) Schematic diagram of the first Brillouin zone (BZ) with high symmetry points and path ($k_x, k_y \in [-\pi, \pi]$).

number of unit cells. A non-zero δm essentially indicates an AM phase. Unless mentioned, throughout the present work, we consider half-filling and express the occupation number being sensitive to both the sublattice and the spin in the form,

$$\langle n_{i\sigma} \rangle = \frac{1}{2} + \begin{cases} +\delta m (-1)^\sigma & i \in \alpha \\ -\delta m (-1)^\sigma & i \in \beta \\ 0 & i \in \gamma \end{cases} \quad (3)$$

where the spin index σ is 0 for \uparrow -spin and 1 for \downarrow -spin. Within the mean-field approximation, the Hubbard term of the Hamiltonian simplifies as $U \sum_{i \in \alpha, \beta} n_{i\uparrow} n_{i\downarrow} \approx \langle n_{i\uparrow} \rangle n_{i\downarrow} + n_{i\uparrow} \langle n_{i\downarrow} \rangle - \langle n_{i\uparrow} \rangle \langle n_{i\downarrow} \rangle$ which can be decoupled as $-U\delta m \left[\sum_{i \in \alpha} (n_{i\uparrow} - n_{i\downarrow}) - \sum_{i \in \beta} (n_{i\uparrow} - n_{i\downarrow}) \right]$ using Eq. (3). We take the Fourier transformation of the Hamiltonian and calculate the order parameter self-consistently with a tolerance of 10^{-5} . Further details of the calculation can be found in the Supplemental Material (SM).

ORDER PARAMETER

We first demonstrate the emergence of AM phase in the minimal model (without any second neighbor hopping) of Lieb-5 lattice through the spin-resolved band structure in Fig. 2(a). Then, we study the effect of the diagonal hopping integral on the AM phase in Fig. 2(b-c). We plot the band structures along paths connecting the high symmetry points of the Brillouin zone (BZ) shown in Fig. 2(d): $\Gamma(0,0) \xrightarrow{k_y=0} X(\pi,0) \xrightarrow{k_x=\pi} M(\pi,\pi) \xrightarrow{k_x=k_y} \Gamma(0,0)$ and its mirror image path. From Fig. 2(a-c), it

is evident that the energy bands are spin-split along Γ - X - M path which encodes two paths parallel to k_x and k_y -axis consecutively (see Fig. 2(d)). In contrast, it shows spin-degeneracy along M - Γ or equivalently Γ - M' path (diagonal path). Comparing the band structure along Γ - X - M - Γ with that for Γ - M' - X' - Γ path, a momentum-inversion symmetry is unraveled, confirming the zero net magnetization in the system. This momentum-dependent spin-splitting, along with the zero net magnetization, indicates the AM phase in the system. It appears both with and without diagonal hopping.

With the onset of the AM phase, we observe that the AM phase emerging in the Lieb-5 lattice is basically an isolated band metal type with a single band around the Fermi energy, maintaining an energy gap from other bands as seen in Fig. 2(a). The appearance of this unique phase is completely different from AM phases found in Lieb metal [87] and also in other lattices [20, 21, 59, 78–85] so far in the literature. We call it altermagnetic isolated band metal (AMIM). Naturally, a question arises about the robustness of the AMIM phase upon the inclusion of the diagonal hopping t_d . As seen in Fig. 2(b), the AMIM phase remains preserved in the presence of the diagonal hopping for the same Hubbard strength. However, the scenario is different when we tune the Hubbard strength. For lower U as shown in Fig. 2(c), while the AM phase is ensured, the AMM emerges instead of the AMIM phase in the presence of the diagonal hopping integral. We get back the AMIM phase in the presence of the diagonal hopping for larger Hubbard strength, confirming the sensitivity of the AM phase to both the Hubbard interaction and hopping strength.

In order to investigate the interplay of the Hubbard strength and the hopping integral, we now analyze the behavior of the AM order parameter δm with Hubbard strength U and the intercell t_2 (diagonal hopping parameter t_d) in Fig. 3(a-b) ((c-d)). The zero δm corresponds to the NM phase (violet region), while the non-zero values of δm indicate two different AM phases: (i) AMM phase with lower amplitudes of δm (green region) and (ii) AMIM phase with higher values of δm (blue region). We confirm the distinction between the two AM phases from the band structure. For a given t_2 , there exists a threshold value of U to obtain the AM phase, e.g. $U_{\text{th}} \sim 1$ for $t_2 = 0.1$. For the Hubbard strength lower than U_{th} , the spin splitting completely disappears, resulting in a normal metallic (NM) phase with zero δm (see Fig. 3(a)). Thus, a *phase transition from the NM to AMIM driven by the Hubbard interaction strength occurs in Lieb-5 lattice without any second-neighbor interaction*, while to get the AM phase in the traditional Lieb lattice with the second nearest neighbor hopping is essential [87]. The reason behind the threshold U_{th} lies in the underlying lattice geometry and the distribution of the order parameter $\pm U\delta m$ among the sublattices and spin configuration. They are proportional to the staggered magnetization, maintaining a distribu-

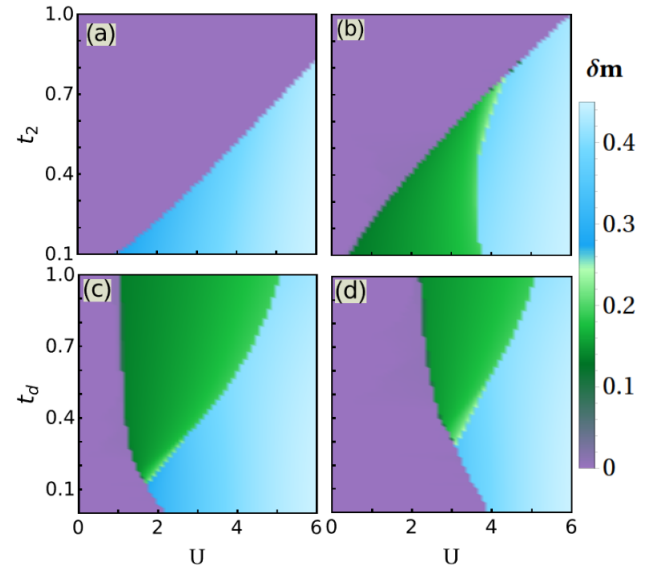


FIG. 3: (a,b) Density plot of δm with Hubbard U and (a-b) intercell hopping integral t_2 for (a) $t_d = 0$, (b) $t_d = 0.5$ and (c-d) diagonal hopping integral for (c) $t_2 = 0.25$, (d) $t_2 = 0.5$. Other parameter values are the same as in Fig. 2.

tion within each unit cell of the lattice geometry. When both the intra and intercell hopping strengths (t_1 and t_2) are comparable, the mobility of the electrons within the lattice increases, bringing the system back to the NM phase for the same Hubbard strength. The staggered on-site configuration gets affected, and the system no longer supports the AM phase. Thus, preserving the AM phase in the system is possible by keeping t_2 always less than t_1 . For a fixed t_1 , the required U_{th} to get the AM phase will be proportional to t_2 . Note that U is constrained in the mean field approximation.

With the inclusion of the diagonal hopping t_d , another metallic phase along with a spin-split configuration, *the AMM phase emerges as an intermediate phase during the transition from the NM to AMIM phase* by tuning the Hubbard strength as shown in Fig. 3(b). The intermediate AMM phase appears because the hopping t_d allows an extra path for the electrons to hop between α and β sublattices within each unit cell, enhancing the mobility of the electrons in the system. In fact, further increasing this intercell hopping integral brings the NM phase back to the system for the given U . The role of t_d behind the appearance of the intermediate AMM phase can be understood more clearly when we plot the phase diagram as a function of t_d keeping t_2 fixed (see Fig 3(c-d)). For a given t_2 , the phase transition from the NM to AMM to AMIM occurs, showing AMM phase for a wide range of U when t_2 is small. Increasing t_2 further will increase the threshold value of t_d to get the AMM phase, as seen by comparing Fig 3(c) and (d). Also, the AMM region of

the phase diagram gets squeezed for higher t_2 . Thus, by tuning t_2 and t_d properly, one can obtain an AMM phase over a large U region in addition to the AMIM phase. Thus, the role of the finite diagonal hopping is dual: (i) it lowers the threshold on U for the emergence of the AM phase and (ii) it renders two consecutive phase transitions, NM to AMM to AMIM, driven by the Hubbard U . We refer to the SM for the full band structures and further discussions. We also calculate δm in the real space as shown in the SM and find excellent agreement with the results in the momentum space.

SPECTRAL FUNCTION

With an understanding of the band structure and phase diagram, we now investigate the spin-resolved spectral function, which is directly related to the angle-resolved photoemission spectroscopy (ARPES) spectra in experiments. It is defined as

$$A_{\uparrow(\downarrow)}(\omega) = \frac{\eta}{\pi} \sum_k \frac{|\langle k | \uparrow(\downarrow) \rangle|^2}{(\omega - (E_k - \mu))^2 + \eta^2}, \quad (4)$$

where ω is the energy of the incoming electron with spin \uparrow (\downarrow) and eigen state $|\uparrow\rangle$ ($|\downarrow\rangle$), $|k\rangle$ is the eigenstate of the system corresponding to the energy E_k , μ is the chemical potential, and η is the spectral broadening factor.

In Fig 4, we plot the difference between the two spectral functions corresponding to the two spins at $\omega = 0$ in the momentum space for different Hubbard strengths in the presence of t_d . These parameter regimes refer to Fig. 2 corresponding to the AMM and AMIM phase, respectively. The difference spectral function $\Delta A(\omega)$ exhibits alternating sign changes along different directions in the k -space with crossings at certain symmetry points following the $[C_4]$ symmetry (see Fig. 4(a)). The nature of alternating sign changes is also preserved in the AMIM phase as shown in Fig. 4(b), indicating a well-defined momentum-dependent spin polarization with d -wave symmetry, inherently favoring AM phases. Before we leave this section, the spin-resolved spectral functions for both up and down spins is also computed along the high-symmetry path for non-zero ω (see SM).

SPIN-ORBIT INTERACTION

In order to examine the stability of the AM phases against the intrinsic spin-orbit coupling (SOC), we compute the spin-resolved band structure of the Lieb-5 lattice by incorporating SOC into the Hamiltonian as [93, 122, 123],

$$H_{\text{SOC}} = i\lambda_{\text{SOC}} \sum_{\langle\langle i,j \rangle\rangle} \nu_{ij} c_i^\dagger \sigma_z c_j + h.c. \quad (5)$$

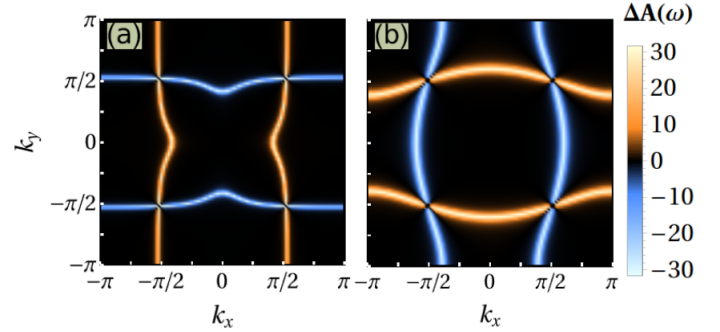


FIG. 4: Spin-resolved spectral function $\Delta A(\omega) = A_{\uparrow}(\omega) - A_{\downarrow}(\omega)$ in k_x, k_y space for Lieb-5 lattice with (a) $U = 3$ and (b) $U = 5$ considering $t_d = 0.5$, $\omega = 0$ and $\eta = 0.01$. The other parameters are the same as in Fig. 2.

where λ_{SOC} is the strength of the SOC. It takes the opposite signs for the up and down spins, and the factor ν_{ij} can choose ± 1 depending on the direction of the hopping within the lattice. Inclusion of the SOC term only modifies the diagonal interaction t_d : $t_d \pm i\lambda_{\text{SOC}}$ depending upon the spin and coupling direction, keeping the other hopping integrals intact. Note that this SOC behaves like an effective internal magnetic field, with directions being opposite for the two spins. However, unlike the external magnetic field, it does not break the time-reversal symmetry, as up and down spin electrons experience opposite effective magnetic fields. Very recently, both the intrinsic and extrinsic spin-orbital altermagnetism have been reported on a square lattice [124].

In Fig. 5, we show the density plot for the AM order parameter over the space spanned by the Hubbard and the SOC strength. Previously, in the absence of the SOC, the NM phase is found in the phase diagram for both $t_d = 0$ and $t_d \neq 0$ when the Hubbard interaction is weak. With the inclusion of the SOC, while the emergence of three phases: NM, AMM, and AMIM, the requirement of the U_{th} remains preserved qualitatively, the magnitude of U_{th} decreases from 3.9 to 2.6 with the increase of the SOC strength. Note that the NM phase found in the presence of the SOC is also an isolated band type, since the bands are separated by energy gaps (see SM for details), with one isolated band appearing around the Fermi energy. Also, there is a tendency of the emergence of AM phase as an intermediate phase (see Fig. 5(a)) even without considering any diagonal hopping. In fact, this intermediate region becomes prominent when we include the diagonal hopping as found in Fig. 5(b). On top of these phenomena, the emergence of the AMIM remains preserved, indicating the stability of the AM phases in the presence of the SOC. We refer to the SM for the discussion on the band topology in the presence of SOC and Hubbard interaction.

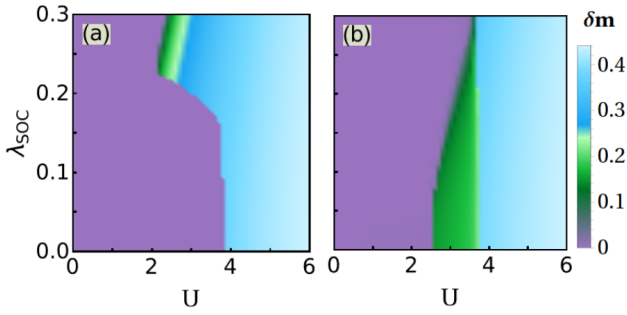


FIG. 5: Density profile of δm over U and SOC (λ_{soc}) for (a) $t_d = 0$ and (b) $t_d = 0.5$. The other parameters are the same as in Fig. 2.

SUMMARY AND CONCLUSIONS

To summarize, we have shown the emergence of spin-lattice symmetric AM phases characterized by the sublattice degree of freedom, specifically, AMM and AMIM, in a repulsive Hubbard model on Lieb-5 lattice. By investigating the spin-resolved band structure, the altermagnetic order parameter, and the spectral function, we demonstrate the phase transition from the NM to either the AMIM or from the NM to AMIM via AMM phase through the phase diagram over a wide parameter space. The classification of the AM phases into the AMM and AMIM phases has been confirmed based on the appearance of the spin-split band structures and the amplitude of the order parameter. A minimum local environment within the lattice has been identified to get the AMM phase being stable against the SOC, along with the additional advantages of lower threshold values of the Hubbard strength. The unique AMIM phase characterized by a single band crossing at the Fermi level and thus resulting in highly suppressed interband scatterings, has made our model promising for applications in quantum device components, particularly for switching operations.

The experimental realization of the Lieb-5 lattice in *Ga*-doped *YIG* layer systems [111], two-dimensional polymers composed of zinc-phthalocyanine (ZnPc) [125], photonics [126, 127] enhances the potential of our proposal. Moreover, the observation of AFM orders in lattice Hubbard models [128–130] and the possibility of implementation of tunability of U via Feshbach resonances [131] further strengthen the potential of our model for the realization of AM phases.

ACKNOWLEDGEMENT

We acknowledge the Department of Space (DoS), Government of India, for all support at Physical Research Laboratory (PRL) and also the ParamVikram-1000 HPC facility at PRL, Ahmedabad, for carrying out a major part

of the calculations. S. B. thanks Arunava Chakrabarti and Muktish Acharyya for some helpful discussions, and Purnendu Das for helpful communication.

* sougatabiswas@prl.res.in

† achintyaa@prl.res.in

‡ paramita@prl.res.in

- [1] S. Hayami, Y. Yanagi, and H. Kusunose, Momentum-dependent spin splitting by collinear antiferromagnetic ordering, *Journal of the Physical Society of Japan* **88**, 123702 (2019).
- [2] L. Smejkal, R. Gonzalez-Hernandez, T. Jungwirth, and J. Sinova, Crystal time-reversal symmetry breaking and spontaneous hall effect in collinear antiferromagnets, *Science advances* **6**, eaaz8809 (2020).
- [3] L.-D. Yuan, Z. Wang, J.-W. Luo, E. I. Rashba, and A. Zunger, Giant momentum-dependent spin splitting in centrosymmetric low- z antiferromagnets, *Phys. Rev. B* **102**, 014422 (2020).
- [4] S. Hayami, Y. Yanagi, and H. Kusunose, Bottom-up design of spin-split and reshaped electronic band structures in antiferromagnets without spin-orbit coupling: Procedure on the basis of augmented multipoles, *Phys. Rev. B* **102**, 144441 (2020).
- [5] L. Smejkal, J. Sinova, and T. Jungwirth, Emerging research landscape of altermagnetism, *Phys. Rev. X* **12**, 040501 (2022).
- [6] L. Smejkal, J. Sinova, and T. Jungwirth, Beyond conventional ferromagnetism and antiferromagnetism: A phase with nonrelativistic spin and crystal rotation symmetry, *Phys. Rev. X* **12**, 031042 (2022).
- [7] I. I. Mazin, K. Koepenik, M. D. Johannes, R. Gonzalez-Hernandez, and L. Smejkal, Prediction of unconventional magnetism in doped fesb2, *Proceedings of the National Academy of Sciences* **118**, e2108924118 (2021).
- [8] Z. Feng, X. Zhou, L. Šmejkal, L. Wu, Z. Zhu, H. Guo, R. Gonzalez-Hernandez, X. Wang, H. Yan, P. Qin, *et al.*, An anomalous hall effect in altermagnetic ruthenium dioxide, *Nature Electronics* **5**, 735 (2022).
- [9] I. Mazin (The PRX Editors), Editorial: Altermagnetism—a new punch line of fundamental magnetism, *Phys. Rev. X* **12**, 040002 (2022).
- [10] L. Smejkal, J. Sinova, and T. Jungwirth, Beyond conventional ferromagnetism and antiferromagnetism: A phase with nonrelativistic spin and crystal rotation symmetry, *Phys. Rev. X* **12**, 031042 (2022).
- [11] L. Smejkal, J. Sinova, and T. Jungwirth, Emerging research landscape of altermagnetism, *Phys. Rev. X* **12**, 040501 (2022).
- [12] L. Smejkal, A. B. Hellenes, R. Gonzalez-Hernandez, J. Sinova, and T. Jungwirth, Giant and tunneling magnetoresistance in unconventional collinear antiferromagnets with nonrelativistic spin-momentum coupling, *Phys. Rev. X* **12**, 011028 (2022).
- [13] R. D. Gonzalez Betancourt, J. Zubacc, R. Gonzalez-Hernandez, K. Geishendorf, Z. Soban, G. Springholz, K. Olejnik, L. Smejkal, J. Sinova, T. Jungwirth, S. T. B. Goennenwein, A. Thomas, H. Reichlova, J. Zelezny, and D. Kriegner, Spontaneous anomalous hall effect arising from an unconventional compensated magnetic phase in

a semiconductor, *Phys. Rev. Lett.* **130**, 036702 (2023).

[14] R. D. Gonzalez Betancourt, J. Zubac, K. Geishendorf, P. Ritzinger, B. Ruuzickova, T. Kotte, J. Zelezny, K. Olejnik, G. Springholz, B. Buchner, *et al.*, Anisotropic magnetoresistance in altermagnetic mnte, *npj Spintronics* **2**, 45 (2024).

[15] J. Krempasky, L. Smejkal, S. D'souza, M. Hajlaoui, G. Springholz, K. Uhlirova, F. Alarab, P. Constantinou, V. Strocov, D. Usanov, *et al.*, Altermagnetic lifting of kramers spin degeneracy, *Nature* **626**, 517 (2024).

[16] I. Mazin, Altermagnetism then and now, *Physics* **17**, 4 (2024).

[17] P. A. McClarty and J. G. Rau, Landau theory of altermagnetism, *Phys. Rev. Lett.* **132**, 176702 (2024).

[18] C. Song, H. Bai, Z. Zhou, L. Han, H. Reichlova, J. H. Dil, J. Liu, X. Chen, and F. Pan, Altermagnets as a new class of functional materials, *Nature Reviews Materials* , 1 (2025).

[19] S. Lee, S. Lee, S. Jung, J. Jung, D. Kim, Y. Lee, B. Seok, J. Kim, B. G. Park, L. Smejkal, C.-J. Kang, and C. Kim, Broken kramers degeneracy in altermagnetic mnte, *Phys. Rev. Lett.* **132**, 036702 (2024).

[20] P. Das, V. Leeb, J. Knolle, and M. Knap, Realizing altermagnetism in fermi-hubbard models with ultracold atoms, *Phys. Rev. Lett.* **132**, 263402 (2024).

[21] Y. Che, H. Lv, X. Wu, and J. Yang, Engineering altermagnetic states in two-dimensional square tessellations, *Phys. Rev. Lett.* **135**, 036701 (2025).

[22] H. G. Giil and J. Linder, Superconductor-altermagnet memory functionality without stray fields, *Phys. Rev. B* **109**, 134511 (2024).

[23] V. Baltz, A. Hoffmann, S. Emori, D.-F. Shao, and T. Jungwirth, Emerging materials in antiferromagnetic spintronics, *APL Materials* **12** (2024).

[24] O. Fedchenko, J. Minar, A. Akashdeep, S. W. D'Souza, D. Vasilyev, O. Tkach, L. Odenbreit, Q. Nguyen, D. Kutyaykhov, N. Wind, *et al.*, Observation of time-reversal symmetry breaking in the band structure of altermagnetic ruo₂, *Science advances* **10**, eadj4883 (2024).

[25] X. Zhou, W. Feng, R.-W. Zhang, L. Smejkal, J. Sinova, Y. Mokrousov, and Y. Yao, Crystal thermal transport in altermagnetic ruo₂, *Phys. Rev. Lett.* **132**, 056701 (2024).

[26] Y. Guo, J. Zhang, Z. Zhu, Y.-y. Jiang, L. Jiang, C. Wu, J. Dong, X. Xu, W. He, B. He, *et al.*, Direct and inverse spin splitting effects in altermagnetic ruo₂, *Advanced Science* **11**, 2400967 (2024).

[27] S.-D. Guo, X.-S. Guo, and G. Wang, Valley polarization in two-dimensional tetragonal altermagnetism, *Phys. Rev. B* **110**, 184408 (2024).

[28] Z. Lin, D. Chen, W. Lu, X. Liang, S. Feng, K. Yamagami, J. Osiecki, M. Leandersson, B. Thiagarajan, J. Liu, *et al.*, Observation of giant spin splitting and d-wave spin texture in room temperature altermagnet ruo₂, arXiv preprint arXiv:2402.04995 (2024).

[29] S. Reimers, L. Odenbreit, L. Smejkal, V. N. Strocov, P. Constantinou, A. B. Hellenes, R. Jaeschke Ubiergo, W. H. Campos, V. K. Bharadwaj, A. Chakraborty, *et al.*, Direct observation of altermagnetic band splitting in crsb thin films, *Nature Communications* **15**, 2116 (2024).

[30] G. Yang, Z. Li, S. Yang, J. Li, H. Zheng, W. Zhu, Z. Pan, Y. Xu, S. Cao, W. Zhao, *et al.*, Three-dimensional mapping of the altermagnetic spin splitting in crsb, *Nature Communications* **16**, 1442 (2025).

[31] J. Ding, Z. Jiang, X. Chen, Z. Tao, Z. Liu, T. Li, J. Liu, J. Sun, J. Cheng, J. Liu, Y. Yang, R. Zhang, L. Deng, W. Jing, Y. Huang, Y. Shi, M. Ye, S. Qiao, Y. Wang, Y. Guo, D. Feng, and D. Shen, Large band splitting in g-wave altermagnet crsb, *Phys. Rev. Lett.* **133**, 206401 (2024).

[32] C. Li, M. Hu, Z. Li, Y. Wang, W. Chen, B. Thiagarajan, M. Leandersson, C. Polley, T. Kim, H. Liu, *et al.*, Topological weyl altermagnetism in crsb, *Communications Physics* **8**, 311 (2025).

[33] M. Naka, S. Hayami, H. Kusunose, Y. Yanagi, Y. Motome, and H. Seo, Spin current generation in organic antiferromagnets, *Nature Communications* **10**, 4305 (2019).

[34] M. Naka, S. Hayami, H. Kusunose, Y. Yanagi, Y. Motome, and H. Seo, Anomalous hall effect in κ -type organic antiferromagnets, *Phys. Rev. B* **102**, 075112 (2020).

[35] I. I. Mazin, Altermagnetism in mnte: Origin, predicted manifestations, and routes to detwinning, *Phys. Rev. B* **107**, L100418 (2023).

[36] T. Osumi, S. Souma, T. Aoyama, K. Yamauchi, A. Honma, K. Nakayama, T. Takahashi, K. Ohgushi, and T. Sato, Observation of a giant band splitting in altermagnetic mnte, *Phys. Rev. B* **109**, 115102 (2024).

[37] S. Bhowal and N. A. Spaldin, Ferroically ordered magnetic octupoles in d-wave altermagnets, *Phys. Rev. X* **14**, 011019 (2024).

[38] J. Nag, B. Das, S. Bhowal, Y. Nishioka, B. Bandyopadhyay, S. Sarker, S. Kumar, K. Kuroda, V. Gopalan, A. Kimura, K. G. Suresh, and A. Alam, Gdalsi: An antiferromagnetic topological weyl semimetal with non-relativistic spin splitting, *Phys. Rev. B* **110**, 224436 (2024).

[39] B. Jiang, M. Hu, J. Bai, Z. Song, C. Mu, G. Qu, W. Li, W. Zhu, H. Pi, Z. Wei, *et al.*, A metallic room-temperature d-wave altermagnet, *Nature Physics* , 1 (2025).

[40] M. Roig, A. Kreisel, Y. Yu, B. M. Andersen, and D. F. Agterberg, Minimal models for altermagnetism, *Phys. Rev. B* **110**, 144412 (2024).

[41] Y. Guo, H. Liu, O. Janson, I. C. Fulga, J. van den Brink, and J. I. Facio, Spin-split collinear antiferromagnets: A large-scale ab-initio study, *Materials Today Physics* **32**, 100991 (2023).

[42] S.-B. Zhang, L.-H. Hu, and T. Neupert, Finite-momentum cooper pairing in proximitized altermagnets, *Nature Communications* **15**, 1801 (2024).

[43] W. Zhao, Y. Fukaya, P. Burset, J. Cayao, Y. Tanaka, and B. Lu, Orientation-dependent transport in junctions formed by d-wave altermagnets and d-wave superconductors, *Phys. Rev. B* **111**, 184515 (2025).

[44] J. A. Ouassou, A. Brataas, and J. Linder, dc josephson effect in altermagnets, *Phys. Rev. Lett.* **131**, 076003 (2023).

[45] D. Chakraborty and A. M. Black-Schaffer, Zero-field finite-momentum and field-induced superconductivity in altermagnets, *Phys. Rev. B* **110**, L060508 (2024).

[46] G. Sim and J. Knolle, Pair density waves and supercurrent diode effect in altermagnets, *Phys. Rev. B* **112**, L020502 (2025).

[47] S. Hong, M. J. Park, and K.-M. Kim, Unconventional p-wave and finite-momentum superconductivity induced by altermagnetism through the formation of bogoliubov fermi surface, *Phys. Rev. B* **111**, 054501 (2025).

[48] D. Debnath, A. Saha, and P. Dutta, Spin-polarization and diode effect in thermoelectric current through altermagnet-based superconductor heterostructures, arXiv preprint arXiv:2509.12198 (2025).

[49] P. O. Sukhachov, E. W. Hodt, and J. Linder, Thermoelectric effect in altermagnet-superconductor junctions, *Phys. Rev. B* **110**, 094508 (2024).

[50] M. Papaj, Andreev reflection at the altermagnet-superconductor interface, *Phys. Rev. B* **108**, L060508 (2023).

[51] D. Zhu, Z.-Y. Zhuang, Z. Wu, and Z. Yan, Topological superconductivity in two-dimensional altermagnetic metals, *Phys. Rev. B* **108**, 184505 (2023).

[52] Y.-X. Li and C.-C. Liu, Majorana corner modes and tunable patterns in an altermagnet heterostructure, *Phys. Rev. B* **108**, 205410 (2023).

[53] S. A. A. Ghorashi, T. L. Hughes, and J. Cano, Altermagnetic routes to majorana modes in zero net magnetization, *Phys. Rev. Lett.* **133**, 106601 (2024).

[54] Y.-X. Li, Realizing tunable higher-order topological superconductors with altermagnets, *Phys. Rev. B* **109**, 224502 (2024).

[55] C. W. J. Beenakker and T. Vakhtel, Phase-shifted andreev levels in an altermagnet josephson junction, *Phys. Rev. B* **108**, 075425 (2023).

[56] Q. Cheng and Q.-F. Sun, Orientation-dependent josephson effect in spin-singlet superconductor/almagnet/spin-triplet superconductor junctions, *Phys. Rev. B* **109**, 024517 (2024).

[57] A. A. Zyuzin, Magnetoelectric effect in superconductors with d -wave magnetization, *Phys. Rev. B* **109**, L220505 (2024).

[58] B. Lu, K. Maeda, H. Ito, K. Yada, and Y. Tanaka, φ josephson junction induced by altermagnetism, *Phys. Rev. Lett.* **133**, 226002 (2024).

[59] A. Bose, S. Vadnais, and A. Paramekanti, Altermagnetism and superconductivity in a multiorbital $t-j$ model, *Phys. Rev. B* **110**, 205120 (2024).

[60] K. Maeland, B. Brekke, and A. Sudbo, Many-body effects on superconductivity mediated by double-magnon processes in altermagnets, *Phys. Rev. B* **109**, 134515 (2024).

[61] J.-X. Hu, O. Matsyshyn, and J. C. W. Song, Nonlinear superconducting magnetoelectric effect, *Phys. Rev. Lett.* **134**, 026001 (2025).

[62] B. Chi, L. Jiang, Y. Zhu, G. Yu, C. Wan, J. Zhang, and X. Han, Crystal-facet-oriented altermagnets for detecting ferromagnetic and antiferromagnetic states by giant tunneling magnetoresistance, *Phys. Rev. Appl.* **21**, 034038 (2024).

[63] F. Liu, Z. Zhang, X. Yuan, Y. Liu, S. Zhu, Z. Lu, and R. Xiong, Giant tunneling magnetoresistance in insulated altermagnet/ferromagnet junctions induced by spin-dependent tunneling effect, *Phys. Rev. B* **110**, 134437 (2024).

[64] L. Del Re, Dirac points and topological phases in correlated altermagnets, *Phys. Rev. Res.* **7**, 033234 (2025).

[65] Y.-X. Li, Y. Liu, and C.-C. Liu, Creation and manipulation of higher-order topological states by altermagnets, *Phys. Rev. B* **109**, L201109 (2024).

[66] L. Bai, W. Feng, S. Liu, L. Šmejkal, Y. Mokrousov, and Y. Yao, Altermagnetism: Exploring new frontiers in magnetism and spintronics, *Advanced Functional Materials* **34**, 2409327 (2024).

[67] K. Sourounis and A. Manchon, Efficient generation of spin currents in altermagnets via magnon drag, *Phys. Rev. B* **111**, 134448 (2025).

[68] R. Gonzalez-Hernandez, L. Šmejkal, K. Vyborny, Y. Yagagi, J. Sinova, T. Jungwirth, and J. Zelezny, Efficient electrical spin splitter based on nonrelativistic collinear antiferromagnetism, *Phys. Rev. Lett.* **126**, 127701 (2021).

[69] D.-F. Shao, S.-H. Zhang, M. Li, C.-B. Eom, and E. Y. Tsymbal, Spin-neutral currents for spintronics, *Nature Communications* **12**, 7061 (2021).

[70] M. Naka, Y. Motome, and H. Seo, Perovskite as a spin current generator, *Phys. Rev. B* **103**, 125114 (2021).

[71] Y. Zhang, H. Bai, L. Han, C. Chen, Y. Zhou, C. H. Back, F. Pan, Y. Wang, and C. Song, Simultaneous high charge-spin conversion efficiency and large spin diffusion length in altermagnetic ruo₂, *Advanced Functional Materials* **34**, 2313332 (2024).

[72] R.-W. Zhang, C. Cui, R. Li, J. Duan, L. Li, Z.-M. Yu, and Y. Yao, Predictable gate-field control of spin in altermagnets with spin-layer coupling, *Phys. Rev. Lett.* **133**, 056401 (2024).

[73] S.-D. Guo, Y. Liu, J. Yu, and C.-C. Liu, Valley polarization in twisted altermagnetism, *Phys. Rev. B* **110**, L220402 (2024).

[74] A. Hariki, A. Dal Din, O. J. Amin, T. Yamaguchi, A. Badura, D. Kriegner, K. W. Edmonds, R. P. Campion, P. Wadley, D. Backes, L. S. I. Veiga, S. S. Dhesi, G. Springholz, L. Šmejkal, K. Vyborny, T. Jungwirth, and J. Kunes, X-ray magnetic circular dichroism in altermagnetic α -mnte, *Phys. Rev. Lett.* **132**, 176701 (2024).

[75] D. Rathore, Altermagnetism: symmetry-driven spin splitting and its role in spintronic technologies, *Journal of Alloys and Compounds* , 181292 (2025).

[76] H. Yan, X. Zhou, P. Qin, and Z. Liu, Review on spin-split antiferromagnetic spintronics, *Applied Physics Letters* **124** (2024).

[77] S. S. Fender, O. Gonzalez, and D. K. Bediako, Altermagnetism: A chemical perspective, *Journal of the American Chemical Society* **147**, 2257 (2025).

[78] S. He, J. Zhao, H.-G. Luo, and S. Hu, Altermagnetism and beyond in the $t-t'-\delta$ fermi-hubbard model, *Phys. Rev. B* **112**, 035108 (2025).

[79] P. M. Consoli and M. Vojta, SU(n) altermagnetism: Lattice models, magnon modes, and flavor-split bands, *Phys. Rev. Lett.* **134**, 196701 (2025).

[80] T. A. Maier and S. Okamoto, Weak-coupling theory of neutron scattering as a probe of altermagnetism, *Phys. Rev. B* **108**, L100402 (2023).

[81] F. Ferrari and R. Valenti, Altermagnetism on the shastry-sutherland lattice, *Phys. Rev. B* **110**, 205140 (2024).

[82] X. Zhu, X. Huo, S. Feng, S.-B. Zhang, S. A. Yang, and H. Guo, Design of altermagnetic models from spin clusters, *Phys. Rev. Lett.* **134**, 166701 (2025).

[83] A. Vijayvargia, E. Day-Roberts, A. S. Botana, and O. Erten, Altermagnets with topological order in kitaev bilayers, *Phys. Rev. Lett.* **135**, 166701 (2025).

[84] T. Sato, S. Haddad, I. C. Fulga, F. F. Assaad, and J. van den Brink, Altermagnetic anomalous hall effect emerging from electronic correlations, *Phys. Rev. Lett.* **133**, 086503 (2024).

[85] S. Giuli, C. Mejuto-Zaera, and M. Capone, Altermagnetism from interaction-driven itinerant magnetism, *Phys. Rev. B* **111**, L020401 (2025).

[86] N. Kaushal and M. Franz, Altermagnetism in modified lieb lattice hubbard model, *Phys. Rev. Lett.* **135**, 156502 (2025).

[87] M. Durrnagel, H. Hohmann, A. Maity, J. Seufert, M. Klett, L. Klebl, and R. Thomale, Altermagnetic phase transition in a lieb metal, *Phys. Rev. Lett.* **135**, 036502 (2025).

[88] J. Liu, X. Mao, J. Zhong, and R. A. Romer, Localization, phases, and transitions in three-dimensional extended lieb lattices, *Phys. Rev. B* **102**, 174207 (2020).

[89] L. O. Lima, J. Faundez, N. C. Costa, and R. R. dos Santos, Finite temperatures and flat bands: The hubbard model on three-dimensional lieb lattices, *Phys. Rev. B* **112**, 125119 (2025).

[90] J. Liu, X. Mao, J. Zhong, and R. A. Romer, Localization properties in lieb lattices and their extensions, *Annals of Physics* **435**, 168544 (2021), special Issue on Localisation 2020.

[91] S. M. Zhang and L. Jin, Flat band in two-dimensional non-hermitian optical lattices, *Phys. Rev. A* **100**, 043808 (2019).

[92] Y. Li, L. Tian, T. Ma, and H.-Q. Lin, Metal-insulator transition in the disordered hubbard model of the lieb lattice, *Phys. Rev. B* **106**, 205149 (2022).

[93] A. Bhattacharya and B. Pal, Flat bands and nontrivial topological properties in an extended lieb lattice, *Phys. Rev. B* **100**, 235145 (2019).

[94] C. Weeks and M. Franz, Topological insulators on the lieb and perovskite lattices, *Phys. Rev. B* **82**, 085310 (2010).

[95] N. Goldman, D. F. Urban, and D. Bercioux, Topological phases for fermionic cold atoms on the lieb lattice, *Phys. Rev. A* **83**, 063601 (2011).

[96] G. Palumbo and K. Meichanetzidis, Two-dimensional chern semimetals on the lieb lattice, *Phys. Rev. B* **92**, 235106 (2015).

[97] F. K. Kunst, G. van Miert, and E. J. Bergholtz, Extended bloch theorem for topological lattice models with open boundaries, *Phys. Rev. B* **99**, 085427 (2019).

[98] C. Li, F. Ye, X. Chen, Y. V. Kartashov, A. Ferrando, L. Torner, and D. V. Skryabin, Lieb polariton topological insulators, *Phys. Rev. B* **97**, 081103 (2018).

[99] S. Banerjee and A. Saxena, Higher chern numbers in multilayer lieb lattices ($\mathcal{N} \geq 2$): Topological transitions and quadratic band crossing lines, *Phys. Rev. B* **103**, 235125 (2021).

[100] K. Noda, K. Inaba, and M. Yamashita, Flat-band ferromagnetism in the multilayer lieb optical lattice, *Phys. Rev. A* **90**, 043624 (2014).

[101] N. C. Costa, T. Mendes-Santos, T. Paiva, R. R. d. Santos, and R. T. Scalettar, Ferromagnetism beyond lieb's theorem, *Phys. Rev. B* **94**, 155107 (2016).

[102] K. Noda, K. Inaba, and M. Yamashita, Magnetism in the three-dimensional layered lieb lattice: Enhanced transition temperature via flat-band and van hove singularities, *Phys. Rev. A* **91**, 063610 (2015).

[103] A. Nikolaenko, P. M. Bonetti, A. Kale, M. Lebrat, M. Greiner, and S. Sachdev, Canted magnetism and F_2 fractionalization in metallic states of the lieb lattice hubbard model near quarter filling, *Phys. Rev. B* **112**, 045129 (2025).

[104] W. Nie, D. Zhang, and W. Zhang, Ferromagnetic ground state of the su(3) hubbard model on the lieb lattice, *Phys. Rev. A* **96**, 053616 (2017).

[105] N. Swain and M. Karmakar, Strain-induced superconductor-insulator transition on a lieb lattice, *Phys. Rev. Res.* **2**, 023136 (2020).

[106] R. P. Penttila, K.-E. Huhtinen, and P. Torma, Flat-band ratio and quantum metric in the superconductivity of modified lieb lattices, *Communications Physics* **8**, 50 (2025).

[107] K. Yamazaki, M. Ochi, D. Ogura, K. Kuroki, H. Eisaki, S. Uchida, and H. Aoki, Superconducting mechanism for the cuprate $\text{Ba}_2\text{CuO}_{3+\delta}$ based on a multiorbital lieb lattice model, *Phys. Rev. Res.* **2**, 033356 (2020).

[108] D. Roman-Cortes, G. Fadic, C. Cid-Lara, D. Guzman-Silva, B. Real, and R. A. Vicencio, Strain induced localization to delocalization transition on a lieb photonic ribbon lattice, *Scientific Reports* **11**, 21411 (2021).

[109] R. A. Vicencio, C. Cantillano, L. Morales-Inostroza, B. Real, C. Mejia-Cortes, S. Weimann, A. Szameit, and M. I. Molina, Observation of localized states in lieb photonic lattices, *Phys. Rev. Lett.* **114**, 245503 (2015).

[110] M. R. Slot, T. S. Gardenier, P. H. Jacobse, G. C. Van Miert, S. N. Kempkes, S. J. Zevenhuizen, C. M. Smith, D. Vanmaekelbergh, and I. Swart, Experimental realization and characterization of an electronic lieb lattice, *Nature physics* **13**, 672 (2017).

[111] G. Centala and J. W. Klos, Compact localized states in magnonic lieb lattices, *Scientific Reports* **13**, 12676 (2023).

[112] C. E. Whittaker, E. Cancellieri, P. M. Walker, D. R. Gulevich, H. Schomerus, D. Vaitiekus, B. Royall, D. M. Whittaker, E. Clarke, I. V. Iorsh, I. A. Shelykh, M. S. Skolnick, and D. N. Krizhanovskii, Exciton polaritons in a two-dimensional lieb lattice with spin-orbit coupling, *Phys. Rev. Lett.* **120**, 097401 (2018).

[113] B. Cui, X. Zheng, J. Wang, D. Liu, S. Xie, and B. Huang, Realization of lieb lattice in covalent-organic frameworks with tunable topology and magnetism, *Nature communications* **11**, 66 (2020).

[114] H. Feng, C. Liu, S. Zhou, N. Gao, Q. Gao, J. Zhuang, X. Xu, Z. Hu, J. Wang, L. Chen, J. Zhao, S. X. Du, and Y. Dou, Experimental realization of two-dimensional buckled lieb lattice, *Nano Letters* **20**, 2537 (2020).

[115] F. Diebel, D. Leykam, S. Kroesen, C. Denz, and A. S. Desyatnikov, Conical diffraction and composite lieb bosons in photonic lattices, *Phys. Rev. Lett.* **116**, 183902 (2016).

[116] N. Lazarides and G. P. Tsironis, Squid metamaterials on a lieb lattice: From flat-band to nonlinear localization, *Phys. Rev. B* **96**, 054305 (2017).

[117] M. J. Ablowitz and J. T. Cole, Topological insulators in longitudinally driven waveguides: Lieb and kagome lattices, *Phys. Rev. A* **99**, 033821 (2019).

[118] F. Scafirimuto, D. Urbonas, M. A. Becker, U. Scherf, R. F. Mahrt, and T. Stoferle, Tunable exciton-polariton condensation in a two-dimensional lieb lattice at room temperature, *Communications Physics* **4**, 39 (2021).

[119] W. Zhu, S. Hou, Y. Long, H. Chen, and J. Ren, Simulating quantum spin hall effect in the topological lieb lattice of a linear circuit network, *Phys. Rev. B* **97**, 075310 (2018).

[120] Z.-H. Yang, Y.-P. Wang, Z.-Y. Xue, W.-L. Yang, Y. Hu, J.-H. Gao, and Y. Wu, Circuit quantum electrodynamics

simulator of flat band physics in a lieb lattice, *Phys. Rev. A* **93**, 062319 (2016).

[121] W. Casteels, R. Rota, F. Storme, and C. Ciuti, Probing photon correlations in the dark sites of geometrically frustrated cavity lattices, *Phys. Rev. A* **93**, 043833 (2016).

[122] C. L. Kane and E. J. Mele, Z_2 topological order and the quantum spin hall effect, *Phys. Rev. Lett.* **95**, 146802 (2005).

[123] W. Beugeling, J. C. Everts, and C. Morais Smith, Topological phase transitions driven by next-nearest-neighbor hopping in two-dimensional lattices, *Phys. Rev. B* **86**, 195129 (2012).

[124] Z.-M. Wang, Y. Zhang, S.-B. Zhang, J.-H. Sun, E. Dagotto, D.-H. Xu, and L.-H. Hu, Spin-orbital alternating magnetism, *Phys. Rev. Lett.* **135**, 176705 (2025).

[125] Y. Zhang, S. Zhao, M. Polozij, and T. Heine, Electronic lieb lattice signatures embedded in two-dimensional polymers with a square lattice, *Chemical Science* **15**, 5757 (2024).

[126] H. Hanafi, P. Menz, A. McWilliam, J. Imbrock, and C. Denz, Localized dynamics arising from multiple flat bands in a decorated photonic lieb lattice, *APL Photonics* **7** (2022).

[127] D. Zhang, Y. Zhang, H. Zhong, C. Li, Z. Zhang, Y. Zhang, and M. R. Belic, New edge-centered photonic square lattices with flat bands, *Annals of Physics* **382**, 160 (2017).

[128] R. A. Hart, P. M. Duarte, T.-L. Yang, X. Liu, T. Paiva, E. Khatami, R. T. Scalettar, N. Trivedi, D. A. Huse, and R. G. Hulet, Observation of antiferromagnetic correlations in the hubbard model with ultracold atoms, *Nature* **519**, 211 (2015).

[129] A. Mazurenko, C. S. Chiu, G. Ji, M. F. Parsons, M. Kanasz-Nagy, R. Schmidt, F. Grusdt, E. Demler, D. Greif, and M. Greiner, A cold-atom fermi–hubbard antiferromagnet, *Nature* **545**, 462 (2017).

[130] R. Jordens, N. Strohmaier, K. Gunter, H. Moritz, and T. Esslinger, A mott insulator of fermionic atoms in an optical lattice, *Nature* **455**, 204 (2008).

[131] C. Chin, R. Grimm, P. Julienne, and E. Tiesinga, Feshbach resonances in ultracold gases, *Rev. Mod. Phys.* **82**, 1225 (2010).

Supplemental Material: Altermagnetic phases and phase transitions in Lieb-5 Hubbard model

Sougata Biswas ¹, Achintyaa ^{1,2}, and Paramita Dutta ¹

¹ Theoretical Physics Division, Physical Research Laboratory, Navrangpura, Ahmedabad-380009, India

² Indian Institute of Technology Gandhinagar, Palaj, Gujarat-382055, India

In this Supplemental material, we present some additional discussions on calculations and some results to support our findings presented in the main text. The AM band structures along the high symmetry paths are discussed in the main text. For completeness, we now discuss the full energy band structures and the total spectral density for different AM phases. Then, we discuss the effect of the temperature on the altermagnetic order parameter for different parameter regimes. Finally, we discuss the band topology by calculating the Berry curvature and the Chern number of each band.

Basis and Hamiltonian

The mean-field Hamiltonian in the momentum space is taken as,

$$H = \sum_k \Psi_k^\dagger \begin{bmatrix} H_{\uparrow}(k) & 0 \\ 0 & H_{\downarrow}(k) \end{bmatrix} \Psi_k \quad (\text{S1})$$

where,

$$H_{\uparrow(\downarrow)}(\mathbf{k}) = \begin{pmatrix} \epsilon_{\alpha\uparrow(\downarrow)} & -t_d & -t_2 e^{ik_y} & -t_d & -t_1 \\ -t_d & \epsilon_{\beta\uparrow(\downarrow)} & -t_d & -t_2 e^{-ik_x} & -t_1 \\ -t_2 e^{-ik_y} & -t_d & \epsilon_{\alpha\uparrow(\downarrow)} & -t_d & -t_1 \\ -t_d & -t_2 e^{ik_x} & -t_d & \epsilon_{\beta\uparrow(\downarrow)} & -t_1 \\ -t_1 & -t_1 & -t_1 & -t_1 & \epsilon_{\gamma\uparrow(\downarrow)} \end{pmatrix} \quad (\text{S2})$$

considering the basis $\Psi_k^\dagger = (c_{k\alpha\uparrow}^\dagger, c_{k\beta\uparrow}^\dagger, c_{k\alpha\uparrow}^\dagger, c_{k\beta\uparrow}^\dagger, c_{k\gamma\uparrow}^\dagger, c_{k\alpha\downarrow}^\dagger, c_{k\beta\downarrow}^\dagger, c_{k\alpha\downarrow}^\dagger, c_{k\beta\downarrow}^\dagger, c_{k\gamma\downarrow}^\dagger)$. The onsite terms are basically, $\epsilon_{\alpha\uparrow,\downarrow} = \mp U\delta m$, $\epsilon_{\beta\uparrow,\downarrow} = \pm U\delta m$ and $\epsilon_{\gamma\uparrow,\downarrow} = 0$.

Calculation of altermagnetic order parameter

Momentum-space calculation: In the main text, we show the altermagnetic order parameter (δm) which is solved using the Hartree-Fock equation self-consistently with a tolerance factor of 10^{-5} ,

$$\begin{aligned} \delta m &= \frac{1}{8N} \sum_k \left\langle \sum_{i\in\alpha} (n_{ki\uparrow} - n_{ki\downarrow}) - \sum_{i\in\beta} (n_{ki\uparrow} - n_{ki\downarrow}) \right\rangle_{HF} \\ &= \frac{1}{8N} \sum_{k,j=1}^{10} \psi_j^\dagger(k) \Lambda \psi_j(k) \cdot f(E_{k,j} - \mu) \end{aligned} \quad (\text{S3})$$

where Λ is $\text{diag}[1, -1, 1, -1, 0, -1, 1, -1, 1, 0]$. $E_{k,j}$, and $\psi_j(k)$ are the j^{th} eigenvalues and eigenvectors of the Hamiltonian, and $f(E_{k,j})$ is the Fermi-Dirac distribution function. The chemical potential μ maintains the total fermionic density of the system: $n = \frac{1}{5N} \sum_{k,j} f(E_{k,j} - \mu)$, where N denotes the total number of k_x, k_y points in the BZ. We maintain the half-filling condition ($n = 1$) throughout the calculation.

Real-space calculation: In addition to the momentum space calculation of δm , we also repeat it in the real space using the same prescription. In the real space, the self-consistency equation of δm takes the form,

$$\begin{aligned} \delta m &= \frac{1}{2N'} \left(\sum_{i\in\alpha} \langle n_{i\uparrow} - n_{i\downarrow} \rangle - \sum_{i\in\beta} \langle n_{i\uparrow} - n_{i\downarrow} \rangle \right) \\ &= \frac{1}{2N'} \sum_{j=1}^{2N} \left[\sum_{i\in\alpha} \Delta_{i,j}^{\uparrow\downarrow} - \sum_{i\in\beta} \Delta_{i,j}^{\uparrow\downarrow} \right] f(E_j - \mu) \end{aligned} \quad (\text{S4})$$

where $\Delta_{i,j}^{\uparrow\downarrow} = (|\psi_{i,j\uparrow}|^2 - |\psi_{i,j\downarrow}|^2)$ with N as the total site index and N' indicating the total number of sub-lattice sites α and β .

In Fig. S1 we compare the behaviors of δm found from the momentum-space and real-space calculations without any SOC. In the absence of the diagonal hopping, the behavior of δm showing the transition from the NM to AMIM phase in the momentum-space shows excellent agreement with the behavior in the real-space for the entire range of U as seen in Fig. S1(a). The difference between the transition points for different t_2 values corroborates with the results shown in the main text. In the presence of the diagonal hopping, the step-like feature of δm with the Hubbard strength as depicted in Fig. S1(b) indicating two consecutive phase transitions, NM to AMM and AMM to AMIM show very good agreement between the momentum-space and real-space calculations. We confirm that the very small discrepancies will be solved by increasing the real-space lattice size. However, due to computational limitations, we have restricted our calculations to the present system size.

We also repeat our calculations in the presence of the SOC and show in Fig. S2 for various values of SOC. Similar to the previous case (without SOC), we found excellent agreements between the momentum-space and real-space calculations in the absence of the diagonal hopping, whereas there is a very slight discrepancy in the presence of the diagonal hopping, which will also decrease with the increase in the system size.

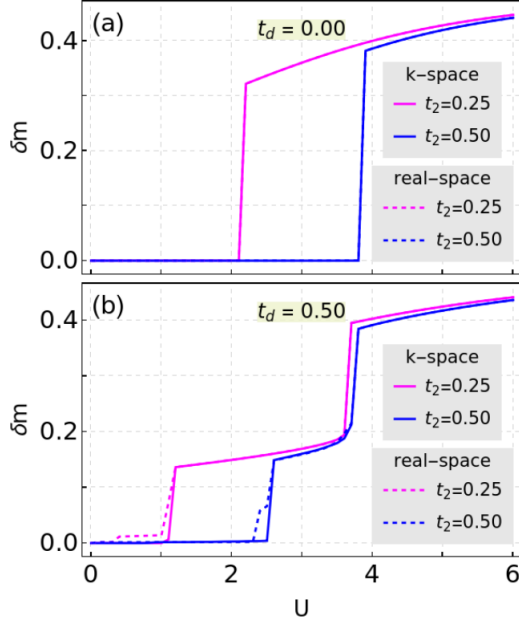


FIG. S1: Variation of δm with the Hubbard interaction strength U for an Lieb-5 lattice with (a) $t_d = 0$ and (b) $t_d = 0.5$. This calculation is performed in both the k -space and real-space ($N = 1620$) for two different values of intercell hopping strength t_2 . Other parameters are kept the same as in Fig. 2.

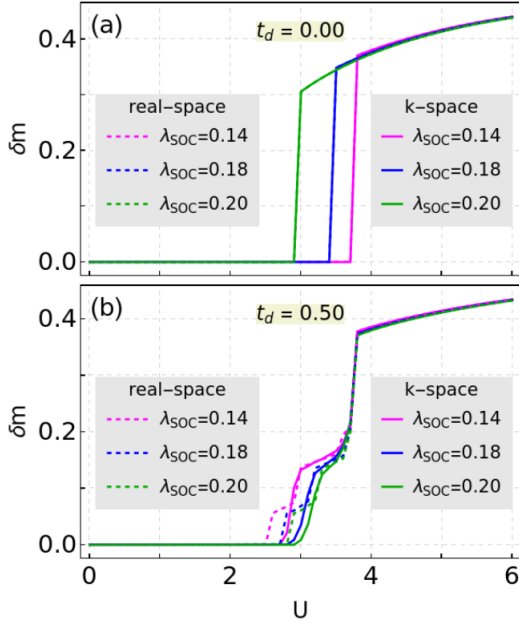


FIG. S2: Behavior of δm with the Hubbard interaction strength U in the presence of SOC, λ_{SOC} for a Lieb-5 lattice with $t_2 = 0.5$ and (a) $t_d = 0$ and (b) $t_d = 0.5$. This calculation is performed in both the k -space and real-space ($N = 1620$). Other parameters are the same as in Fig. 2.

In both Fig. S1 and Fig. S2, the zero δm indicates the default NM phase of the present lattice, or equivalently, the absence of AM phase. δm rises to finite value when the AM phase appears. Now, the transitions from the NM to AMM and AMIM phases are further identified from the two-step behaviors of the AM order parameter. With the introduction of SOC, the threshold value of U i.e., U_{th} decreases with the increase in the SOC strength. Interestingly, the AMIM phase remains almost unaffected by the strong SOC.

Band structures

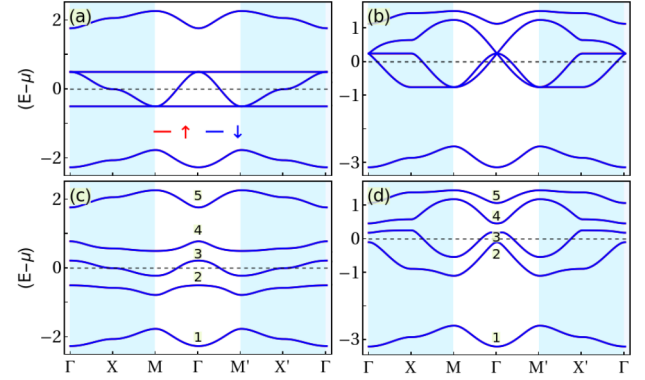


FIG. S3: (a,b) Spin-resolved band structure of Lieb-5 lattice (a-b) without and (c-d) with SOC. The diagonal hopping integral is taken as (a,c) $t_d = 0$ and (b,d) $t_d = 0.5$. The strength of the SOC and Hubbard interaction is fixed as $\lambda_{\text{SOC}} = 0.14$ and $U = 1.5$. The other parameters are the same as in Fig. 2.

In Fig. S3, we present the band structure for a lower Hubbard strength. It shows the normal phases without any spin-splitting. Note that, in the absence of the SOC, a band touching is observed around the Fermi energy for both $t_d = 0$ (see Fig. S3(a)) and $t_d = 0.5$ (see Fig. S3(b)) regimes. Moreover, with the inclusion of the SOC, the bands get separated from each other, but still without any spin-splitting. Corresponding band structures around the high symmetry path are depicted in Fig. S3(c,d). For the better understanding, we also compute the full band structure in the k_x , k_y space as depicted in Fig. S4 and confirm the appearance of spin-degenerate energy bands and the effect of SOC.

The appearance of AM phases is already discussed in the main text, and corresponding spin-resolved bands along the symmetry path are shown in Fig. 2. For completeness, we plot the corresponding spin-resolved band dispersion for the full BZ in Fig. S5. The momentum-dependent splitting of energy bands is apparent for both $t_d = 0$ (see Fig. S5(a)) and $t_d = 0.5$ (see Fig. S5(b,c)) with different Hubbard interaction strengths.

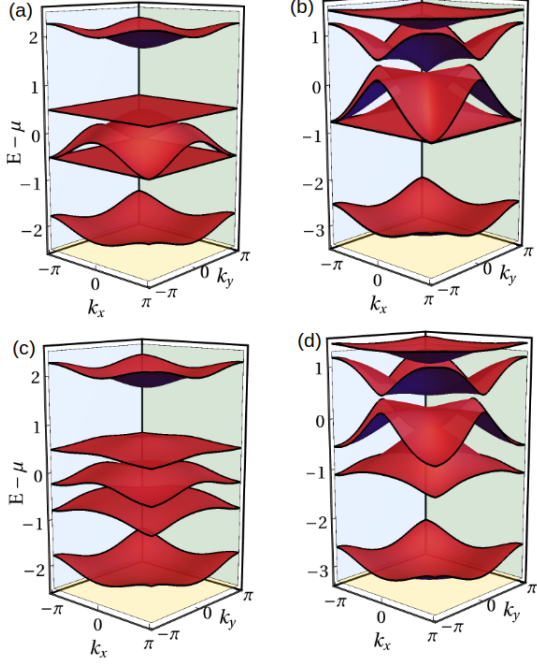


FIG. S4: Energy band dispersion of the Lieb-5 systems (a,b) without and (c,d) with inclusion of SOC, $\lambda_{\text{SOC}} = 0.14$. The diagonal hopping t_d chosen for (a,c) $t_d = 0$ and for (b,d) $t_d = 0.5$. The Hubbard interaction strength is set at $U = 1.5$. Red (blue) colors are strands for spin up (down) bands. Other parameters remain fixed the same as in Fig. 2.

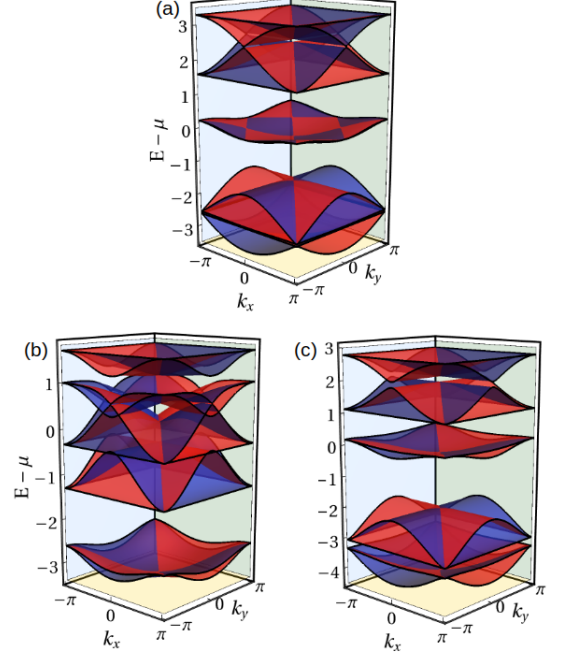


FIG. S5: Energy band structure of the Lieb-5 systems (a) without and (b,c) with the presence of diagonal hopping $t_d = 0.5$. The Hubbard interaction strength is set at (a,c) $U = 5$ and (b) $U = 3$. Red (blue) colors are strands for spin up (down) bands. Other parameters remain fixed the same as in Fig. 2.

Recently, these momentum-dependent energy bands have been realized in various materials using high-resolution ARPES [15, 19, 24, 30, 32].

In addition to the band structure, the behavior of the spectral function is also shown in the main text, but in terms of the difference between the spin components. Here, we calculate the total and the difference spectral density $A_t(\omega) = A_{\uparrow}(\omega) + A_{\downarrow}(\omega)$ along the high-symmetry paths for a fixed energy range ω using Eq. 4 and display in Fig S6. Fig. S6(a) and (b) are shown for different U strengths, which indicate the AMM and AMIM phase, respectively. In Fig. S6(c,d), we compute the difference in spin-resolved spectral density $\Delta A(\omega) = A_{\uparrow}(\omega) - A_{\downarrow}(\omega)$ along the symmetry path. When ω is very close to the own energy of the system, $A_t(\omega)$ appears with a higher amplitude and vanishing values otherwise. Due to this feature, $A_t(\omega)$ creates a bright intensity over the symmetry path around the location of the system's energy, showing a fantastic agreement with the energy band diagram. Noteworthy, the spin-polarization around the $\Gamma - X - M$ (or equivalently $M' - X' - \Gamma$) path is observed with a momentum inversion, whereas $\Delta A(\omega)$ is always zero around the $M - \Gamma - M'$, indicating no spin-polarization.

Effect of Temperature

Till now, we have considered the temperature $T = 0$ for all the results. From a realistic point of view, the stability of AM phases at finite temperatures is an important question to be addressed. Fig. S7 shows the temperature dependence of the δm for various parameter values both in the absence and presence of the SOC. Let us first discuss the scenario without any SOC (solid curves of Fig. S7). In the absence of the diagonal hopping, the emergence of the AMIM phase is only allowed. Now, with increasing temperature, the AM order parameter δm gradually decreases and goes to zero at a critical temperature beyond which the system loses its AM character. Moreover, when the diagonal term is introduced, two AM phases appear. Among these, the lower δm corresponding to the AMM phase also decreases with temperature and goes to zero at different T_c compared to the other phase transition. The AMIM phase with a higher amplitude of δm also follows a similar behavior, showing a higher T_c compared to the AMM phase. To further validate our results, we compute the temperature dependence of δm for all phases after including SOC (dotted lines of Fig. S7). The nature of δm with temperature is largely unaffected for AMIM phases. Under SOC, the amplitude of δm for the AMM

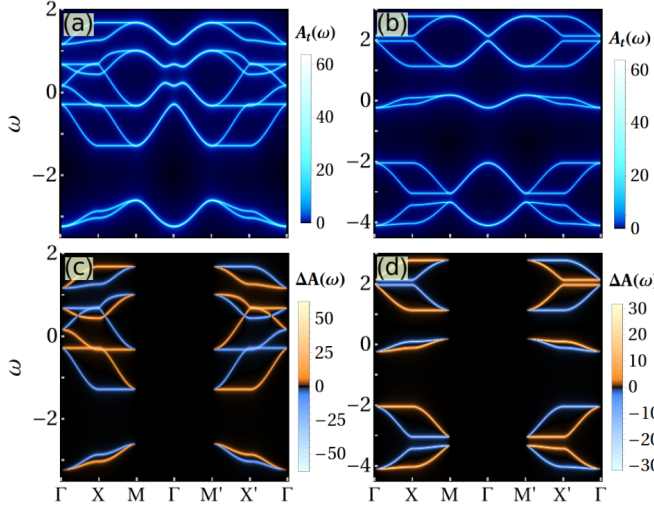


FIG. S6: Visualization of (a,b) total spectral density $A_t(\omega) = A_\uparrow(\omega) + A_\downarrow(\omega)$, (c,d) difference in spin-resolved spectral density $\Delta A(\omega) = A_\uparrow(\omega) - A_\downarrow(\omega)$ over a trial energy range ω along high symmetry path for the Lieb-5 system with (a,c) $U = 3$ and (b,d) $U = 5$. The other parameters are the same as in Fig. 4.

phase contains lower values compared to the AMM phase without SOC. However, their T_c remains the same.

Band Topology

The SOC of the lattice separates all energy bands from each other, which opens the possibility to examine the band topology. In the literature, the band topology has been explored previously in the absence of U [93]. We now compute the Berry curvature and Chern number associated with each band for finite U and t_d , and show in Fig. S8. The Berry curvature associated with n -th band can be defined as,

$$\mathcal{B}(E_n, \mathbf{k}) = \sum_{E_m (\neq E_n)} \frac{-2 \operatorname{Im} \left[\langle \psi_n(\mathbf{k}) | \Delta_x | \psi_m(\mathbf{k}) \rangle \langle \psi_m(\mathbf{k}) | \Delta_y | \psi_n(\mathbf{k}) \rangle \right]}{(E_n - E_m)^2}, \quad (\text{S5})$$

where $\Delta_{x(y)} = \frac{\partial(\mathbf{k})}{\partial k_{x(y)}}$ with H_{tot} as the effective Hamiltonian including SOC and $\psi_n(k)$ as the eigenstate associated with energy E_n for the n -th band. Additionally, the integration of Berry curvature over the first BZ gives the Chern number as,

$$\mathcal{C}_n = \frac{1}{2\pi} \int_{-\pi}^{\pi} \mathcal{B}(E_n, \mathbf{k}) d\mathbf{k}. \quad (\text{S6})$$

Note that, this Chern number is ill-defined when bands touch each other. Thus, the SOC is essential for Lieb-5 lattice for the present calculation.

In the presence of the SOC, when no diagonal hopping is taken into consideration, the Chern number for each band turns out as $\mathcal{C}_n^{\uparrow(\downarrow)} = (0(0), +1(-1), 0(0), -1(+1), 0(0))$, where the band index is mentioned from the lower to higher energy, as marked in Fig. S3(c). Thus, 2nd and 4th bands show a non-trivial topology, and the corresponding distribution of Berry curvature for topologically non-trivial spin-up bands is shown in Fig. S8(a,b). We show it only for one spin because of the degeneracy. Interestingly, as soon as we include the diagonal hopping, the picture of the band topology changes. Explicitly, 3rd and 4th bands exhibit non-trivial topological features,

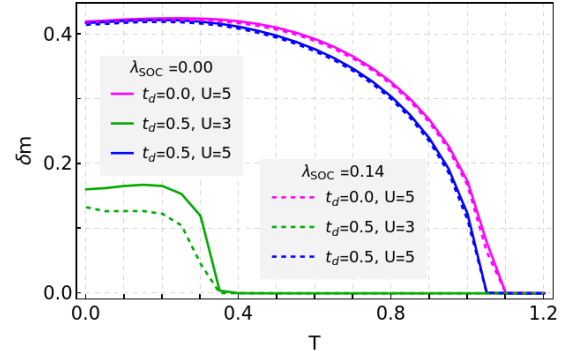


FIG. S7: Variation of AM order parameter with temperature for without and with SOC for various parameter values. The rest of the parameter values are taken same as in Fig. 2.

$\mathcal{C}_n^{\uparrow(\downarrow)} = (0(0), 0(0), -1(+1), +1(-1), 0(0))$ (see Fig. S3(d) for identifying the band index). Corresponding Berry curvature distributions are depicted in Fig. S8(c,d). So, under SOC without any diagonal hopping term $t_d = 0$, the phase transition happens from a topologically non-trivial phase to the AMIM phase, whereas the system permits a

phase transition from the topological non-trivial phase to the AMIM phase by crossing an AMM phase for $t_d \neq 0$.

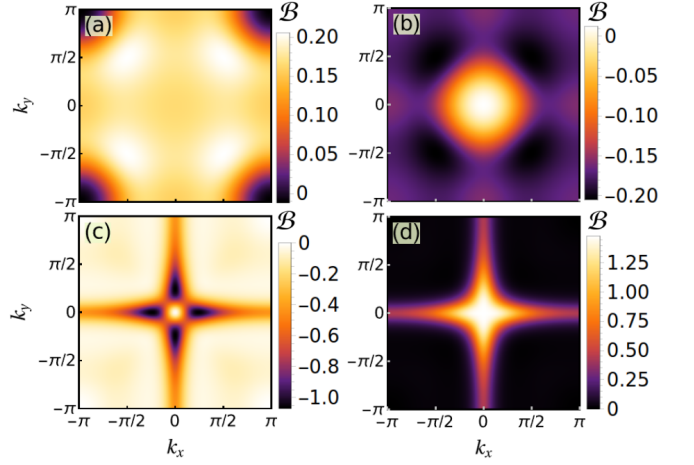


FIG. S8: Behavior of up-spin Berry curvature over the first BZ considering $\lambda_{\text{SOC}} = 0.14$, (a-b) $t_d = 0$ and (c-d) $t_d = 0.5$ for (a) 2nd band ($\mathcal{C}_2^{\uparrow} = 1$), (b) 4th band ($\mathcal{C}_4^{\uparrow} = -1$), (c) 3rd band ($\mathcal{C}_3^{\uparrow} = -1$), and (d) 4th band ($\mathcal{C}_4^{\uparrow} = 1$). The Hubbard interaction strength is taken as $U = 1.5$ and the other parameters are the same as in Fig. 2.